

# Sandwich Plates Actuated by a Kagome Planar Truss

N. Wicks

J. W. Hutchinson

Division of Engineering and Applied Sciences,  
Harvard University,  
Cambridge, MA 02138

*Kagome truss plates have properties that suggest they should be uniquely effective as an actuation plane for sandwich plates: a Kagome truss plate has in-plane isotropy, optimal stiffness and strength, and its truss members can be actuated with minimal internal resistance. In this paper, sandwich plates are studied that are comprised of one solid face sheet and one actuated Kagome face sheet joined by a pyramidal truss core. Various aspects of the actuation behavior of these plates are investigated, including internal resistance and strains resulting from actuation and efficiency of actuation. Single and double curvature actuation modes are investigated. Contact is made with analytic results for actuation modes with long wavelength. [DOI: 10.1115/1.1778720]*

## 1 Introduction

Recent studies of planar trusses based on the ancient Kagome basket weave pattern have shown that these truss plates have many properties that make them desirable for actuation planes of sandwich plates, [1,2]. In this study, we begin by analyzing the actuation characteristics of a single Kagome truss plate (Fig. 1) and follow with an actuation analysis of a sandwich plate comprised of one solid face sheet and one actuated Kagome face sheet joined by a pyramidal truss core (Fig. 2).

The single Kagome truss plate can be constructed from the unit cell shown in Fig. 1(b). The 120 deg symmetry of the structure ensures in-plane elastic isotropy assuming all the truss members are identical. Here, only solid circular members are considered, of length  $L$  and radius  $R$ . The Kagome-backed solid skin plate can be constructed from the unit cell depicted in Fig. 2(c). In the present study we limit consideration to plates with identical solid circular truss members of length  $L$  and radius  $R$  both for the Kagome face and the core. The solid skin thickness is denoted by  $t$ . In addition, to further limit the number of parameters in the system, we consider only plates in which both face sheets and the core members are constructed of the same material with Young's modulus  $E$ , Poisson's ratio  $\nu$  and yield stress  $\sigma_Y$ . The Kagome-backed sandwich plate in Fig. 2 has isotropic bending and stretching stiffness.

The feature of the planar Kagome truss in Fig. 1 that makes it most advantageous for actuation is the ability to actuate members to achieve arbitrary in-plane nodal displacements with minimal internal resistance. Among infinite isotropic planar truss structures, a pin jointed planar Kagome truss is optimally stiff and strong to overall stressing. Although it has kinematic mechanisms, it is nevertheless able to carry arbitrary states of overall stress. Members of a pin jointed Kagome truss can be actuated (i.e., elongated or shortened) with no internal resistance, or equivalently, with no redundant stresses. When joints are welded, as will be assumed throughout this paper, actuation of a member does encounter internal resistance, but minimally so as will be shown. Welded joints also suppress the kinematic mechanisms and result in a structure with substantial in-plane buckling resistance. These and other aspects of the Kagome structure are explored elsewhere, [1–5].

In this study, we aim to explore the details of actuation of the planar Kagome truss and the Kagome-backed sandwich plate.

Contributed by the Applied Mechanics Division of THE AMERICAN SOCIETY OF MECHANICAL ENGINEERS for publication in the ASME JOURNAL OF APPLIED MECHANICS. Manuscript received by the ASME Applied Mechanics Division, October 15, 2003; final revision, January 14, 2004. Associate Editor: R. M. McMeeking. Discussion on the paper should be addressed to the Editor, Prof. Robert M. McMeeking, Journal of Applied Mechanics, Department of Mechanical and Environmental Engineering, University of California–Santa Barbara, Santa Barbara, CA 93106-5070, and will be accepted until four months after final publication of the paper itself in the ASME JOURNAL OF APPLIED MECHANICS.

Simulations of various periodic actuation modes of these infinite Kagome structures have been performed for a range of member aspect ratios. In its most general form, the approach is numerical. A calculation requires the formulation of a “super element” representing a unit cell followed by the assembly of the complete structure as a union of the super elements. The scaling of the energy required for actuating the unloaded structure with aspect ratio of the truss members is investigated. Bending and stretching strains in the members induced by actuation are also determined. For actuation modes with wavelengths long compared to the member length, the response computed with the numerical approach is compared to actuation predicted by an analytical long wavelength approximation outlined in a previous study, [1].

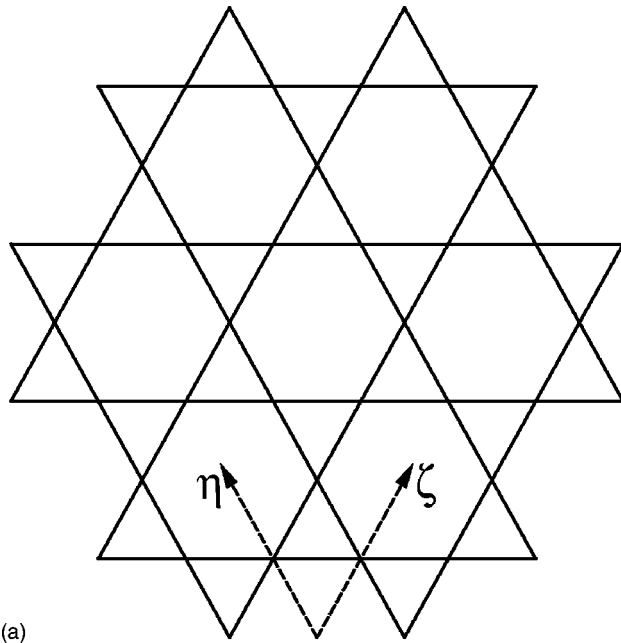
## 2 Planar Kagome Structure

**2.1 The Planar Kagome Structure.** Consider the infinite planar Kagome structure shown in Fig. 1(a) having members of length  $L$  and solid circular cross-sections of radius  $R$  and undergoing in-plane displacements. The unit cell of such a structure is shown in Fig. 1(b). The members are modeled as Euler-Bernoulli beams, with clamped conditions at each node representing welded joints (i.e., the displacement and rotational degrees-of-freedom are the same for all beams meeting at a given node). Actuation of any member comprises an elongation or contraction of the member by a strain  $e$  if the member were unconstrained. In other words, the actuation strain  $e$  is equivalent to a stress-free transformation strain.

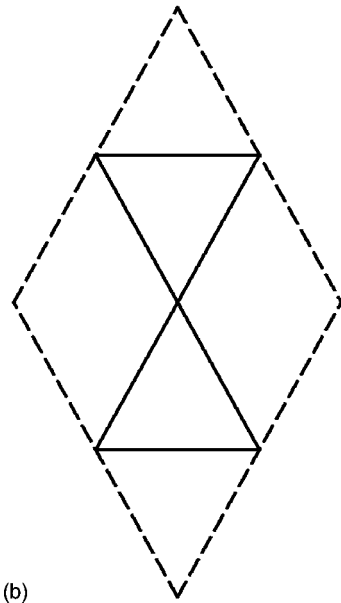
**2.2 Actuation Methodology.** The actuation of beam members is modeled via the so-called cut-stress-reweld scheme employed by Eshelby in his study of the transformation strains in ellipsoidal inclusions, [6]. To actuate a given member, envision the following steps:

1. Remove the actuating member from the structure.
2. Allow the member to actuate (elongate or contract) freely by strain  $e$ .
3. Place equal and opposite forces  $-E\pi R^2 e$  on the ends of the member to deform it back to its original configuration.
4. Place the member back into the structure and “weld” it in place.
5. Release the forces from the ends of the member by applying equal and opposite forces  $E\pi R^2 e$  to the joints at the member ends.

Thus, the cut-stress-reweld procedure is equivalent to analyzing the complete truss subject to equal and opposite actuation forces of magnitude  $E\pi R^2 e$  applied to the joints at the ends of the respective member.



(a)



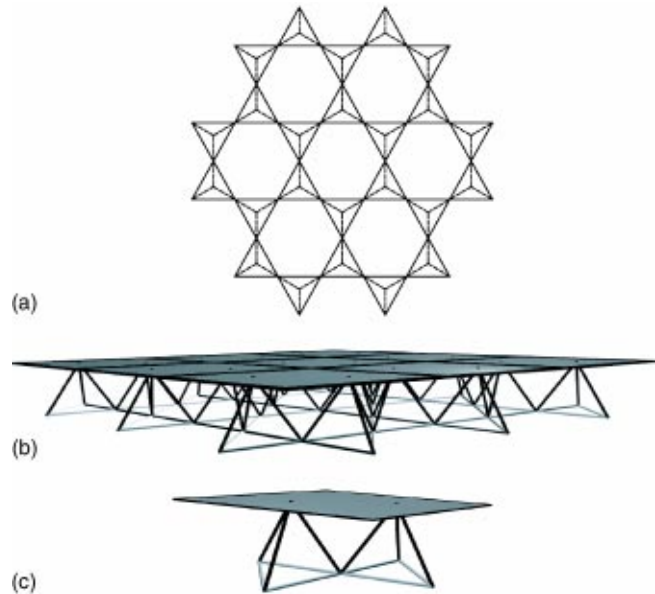
(b)

**Fig. 1 (a) The Kagome planar truss. (b) The unit cell used for the Kagome planar truss analysis. The dashed lines are the outline of the cell. The solid lines are truss members of the unit cell.**

**2.3 Enforcement of Periodicity.** Our goal is to simulate periodic actuations of an infinite structure by modeling the behavior of just one periodic cell subject to periodic boundary conditions. Consider the potential energy functional for a periodic cell:

$$\Phi = \frac{1}{2} K_{ij} u_i u_j - k_j^0 u_j \quad (1)$$

where  $\mathbf{K}$  is the conventional stiffness matrix of the structure,  $\mathbf{u}$  is the vector of displacements and rotations at the nodes of the structure, and  $\mathbf{k}^0$  is the vector of applied nodal forces and moments (in this situation these correspond to the virtual actuation forces described earlier). If the structure were isolated and unconstrained



(a)

(b)

(c)

**Fig. 2 (a) The Kagome plane and tetrahedral core of the Kagome plate structure. The solid members are the Kagome face members, and the dashed members the tetrahedral core members. (b) The Kagome plate structure. (c) The unit cell used for the Kagome plate analysis.**

(apart from rigid-body motion), the problem would be solved in the usual manner by solving the system of equations represented by

$$K_{ij} u_j = k_i^0 \quad (2)$$

Now consider periodic boundary conditions represented by constraints of the form

$$a_{ij} u_j = 0 \quad (3)$$

The details of the actual periodic boundary conditions imposed for in-plane nodal displacements and rotations are included in the Appendix. It is important to note that once the appropriate periodic boundary conditions are imposed on the *displacements/rotations*, periodicity of *forces/moments* is satisfied by the solution. For the periodic cell in Fig. 3, the forces acting on a node along one edge of the periodic cell (corresponding to internal forces in the structure) will be equal and opposite to those acting on the equivalent node on the opposite edge, for a displacement field which satisfies the periodic conditions outlined in the Appendix. The displacements themselves are not, in general, periodic—we consider, for example, a displacement field corresponding to a constant strain. Thus, there are some cases for which the strains, forces and moments, will be periodic, but not the displacements.

To impose these additional conditions, Lagrangian multipliers are employed. The modified energy functional now takes the form:

$$\Phi = \frac{1}{2} K_{ij} u_i u_j - k_j^0 u_j - \lambda_i a_{ij} u_j \quad (4)$$

The systems of equations resulting from minimization of the energy functional with respect to displacements  $u_i$  and the Lagrangian multipliers  $\lambda_i$  are

$$K_{ij} u_j = k_i^0 + \lambda_j a_{ji} \quad (5)$$

$$a_{ij} u_j = 0 \quad (6)$$

Now consider periodic actuations of the infinite structure. The actuation forces exert no net force or moment on the structure.

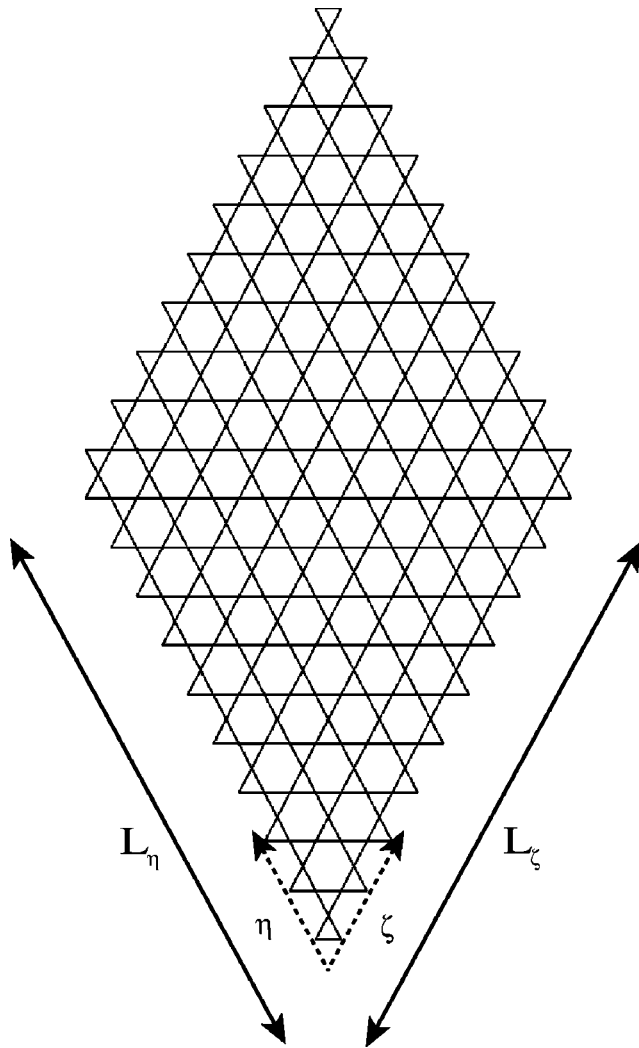


**Fig. 3 The periodic cell used for the planar Kagome truss simulations**

This means that if the energy functional given by (4) above is minimized over the periodic cell, the energy of the infinite structure is also minimized. Thus, it is possible to simulate the behavior of the infinite structure by modeling just the periodic cell with the appropriate boundary conditions.

**2.4 Calculation of Actuators.** The objective is to probe how effectively the planar Kagome structure can achieve arbitrary in-plane deformations through actuation of its members. To this end, periodic actuation of the structure is simulated as described in previous sections for actuation of each member in the periodic cell, tracking the nodal displacements in a matrix of influence coefficients,  $A$ . The  $ij$ th component of this matrix is the  $i$ th displacement resulting from the actuation of the  $j$ th member. To generate this matrix, displacements are calculated at each of the nodes in the periodic cell resulting from a unit actuation of each member in that cell.

As this simulation is linear, once the matrix of influence coefficients,  $A$ , has been constructed, the displacements of the nodes from actuation of any combination of members is easily computed as

$$u_i = A_{ij} e_j \quad (7)$$

where  $\mathbf{e}$  is a vector of member actuators.

Now consider a target field of in-plane nodal displacements  $\mathbf{u}^d$ . The aim is to determine how well this field can be recreated by actuating members of the Kagome structure. Calculate elongations  $\tilde{\mathbf{e}}$  and displacements  $\tilde{\mathbf{u}}$  via the relations:

$$\tilde{e}_i = A_{ij}^\dagger u_j^d \quad (8)$$

$$\tilde{u}_i = A_{ij} \tilde{e}_j \quad (9)$$

where  $A^\dagger$  is the Moore-Penrose generalized inverse of  $A$ , also called the pseudo-inverse of  $A$ , [7]. Then,  $\tilde{\mathbf{e}}$  is the vector of member actuators which minimize the squared error between  $\tilde{\mathbf{u}}$  and  $\mathbf{u}^d$ . If there exist multiple vectors of actuators that minimize this squared error,  $\tilde{\mathbf{e}}$  is such a vector of minimal length (i.e.,  $\|\tilde{\mathbf{e}}\|$  is minimized).

**2.5 Example Target Displacement Fields.** The simulations outlined above were run for several target displacement fields. The objective is to assess the ability of the structure to achieve specific actuators and to determine the associated energy required and stresses induced. The periodic cell used for these simulations is shown in Fig. 3. It contains a total of 100 unit cells. The axes used for describing the displacements fields described here are the  $\zeta$ -axis and the  $\eta$ -axis shown in Fig. 3. It is important to note that the target displacement fields are all consistent with the periodic displacement boundary conditions.

The first target displacement field is described by

$$\mathbf{u}^d = A_0 \mathbf{e}_\zeta \sin\left(\frac{\pi \zeta}{L_\zeta}\right) \quad (10)$$

Here,  $A_0$  is an amplitude factor,  $\mathbf{e}_\zeta$  is a unit vector aligned with the  $\zeta$ -axis, and  $L_\zeta$  the length of the periodic cell in the  $\zeta$ -direction. This target field is a displacement in the  $\zeta$ -direction that is everywhere positive except along the edges  $\zeta=0$  and  $\zeta=L_\zeta$  of the periodic cell where it is zero and reaches a maximum of  $A_0 \mathbf{e}_\zeta$  along the line  $\zeta=L_\zeta/2$  of each periodic cell. In this case, the displacement field is repeated in every periodic cell. This target field is depicted in Fig. 4. The Moore-Penrose best-fit actuators for this displacement field are calculated as described above. For this periodic cell, the number of nodal displacements in the target field is 640, while the number of members actuated is 600. One would expect some error between the target and achievable fields, however the actual displacements differ from the target displacements by less than 1% of the maximum target displacement. The actuators are quite close to the actuators predicted by the long wavelength approximation outlined in previous work, [1]. In this long wavelength theory, the actuation strain,  $\epsilon^T$ , of a member connecting neighboring nodes  $I$  and  $J$  is  $\epsilon^T = (u_\alpha^d(\mathbf{x}^I) - u_\alpha^d(\mathbf{x}^J)) t_\alpha / L$  where  $t_\alpha$  is the unit vector parallel to the member and directed from  $J$  to  $I$  and  $u_\alpha$  is the displacement derived from the target displacement field.

A second target displacement field is described by:

$$\mathbf{u}^d = A_0 (\mathbf{e}_\zeta + \mathbf{e}_\eta) \sin\left(\frac{\pi \zeta}{L_\zeta}\right) \sin\left(\frac{\pi \eta}{L_\eta}\right) \quad (11)$$

Here,  $\mathbf{e}_\eta$  is a unit vector aligned with the  $\eta$ -axis and  $L_\eta$  the length of the unit cell in the  $\eta$  direction. This displacement is zero along all of the edges of the periodic cell and reaches a maximum of  $A_0 (\mathbf{e}_\zeta + \mathbf{e}_\eta)$  at the center ( $\eta=L_\eta/2, \zeta=L_\zeta/2$ ) of each periodic cell. The target displacement field can be seen in Fig. 5. The Moore-Penrose best-fit actuators are predicted quite well by the long wavelength approximation. In this example, the maximum discrepancy between the actual displacements of the nodes and the target displacements is less than 2% of the maximum target displacement. For simulations run for a target displacement field in the same direction, but with a wavelength half of that of (11) (in both the  $\zeta$  and  $\eta$  directions), this maximum discrepancy is less than  $10^{-7}$ . The critical difference between the two sets of target displacement fields is that the field described by (11) with the full wavelength has a jump in slope across the boundaries between

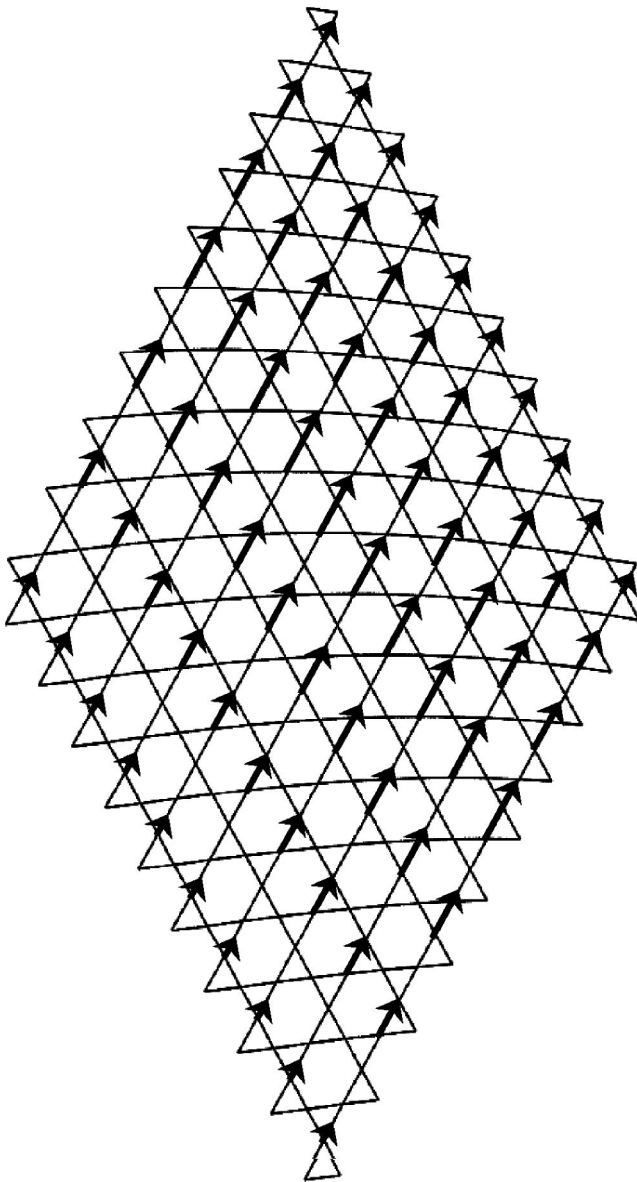


Fig. 4 The target field described by  $u^d = A_0 e_\zeta \sin(\pi \zeta / L_\zeta)$ . The arrows show the displacement vectors of the nodes.

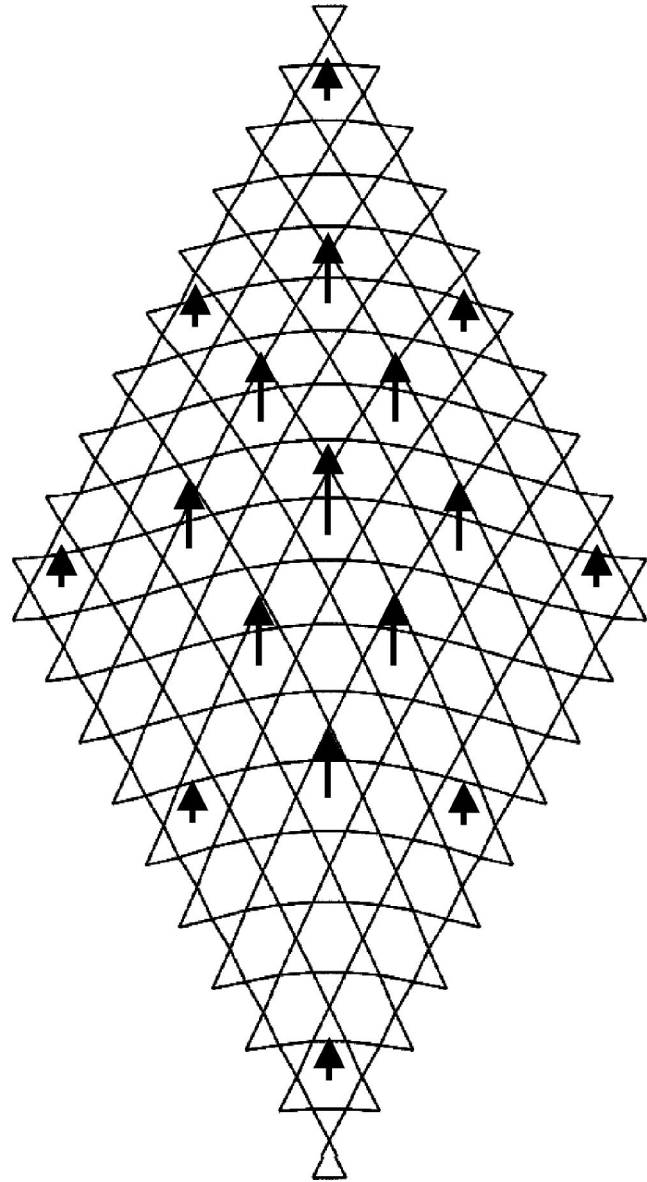


Fig. 5 The target displacement field described by  $u^d = A_0 (e_\zeta + e_\eta) \sin(\pi \zeta / L_\zeta) \sin(\pi \eta / L_\eta)$ . The arrows show the displacement vectors of the nodes.

periodic cells (and, as a result, a jump in actuation). For the displacement field with the half-wavelength, the slope of displacement is continuous across periodic cell boundaries.

A final target displacement field of interest is described by

$$\mathbf{u}_d = A_0 \zeta \mathbf{e}_\zeta. \quad (12)$$

This corresponds to a constant strain of  $A_0$  in the  $\zeta$  direction. This field is shown in Fig. 6. In this example, the actual displacements of the nodes match the target displacements almost perfectly—the maximum discrepancy is less than  $10^{-7}$  of the maximum target displacement. Note that for this displacement field, the slope of displacement is again continuous across periodic cell boundaries.

**2.6 Actuation of Selected Kagome Members.** In practical applications it will generally be desirable to manufacture structures in which only a small subset of the members will be actuated. The Moore-Penrose actuation scheme can be applied in a similar manner in such cases. This procedure is outlined in Section 4.4 for the Kagome plate structure. Given a restriction on the number of members to be actuated, systematic procedures for

identifying the “best” subset of actuation members remain to be established. The behavior of planar Kagome structures with limited numbers of actuation members will be considered in subsequent work.

### 3 Energy of Actuation of Planar Kagome Structure

**3.1 Energy of Actuation.** One of the motivations behind the selection of the Kagome structure for actuation is the desire to find a structure that can be actuated with minimal internal resistance to actuation. Here, we present the total strain energy stored in the planar Kagome structure actuated to achieve the target displacement fields described above. In the limit of a pin-jointed Kagome structure, actuations can be achieved with no internal resistance, although mechanisms will also exist, [1]. For the Kagome structures considered here, simulated with Euler-Bernoulli beams welded together at their ends, the energy of actuation is expected to be due primarily to elastic bending of the beams.

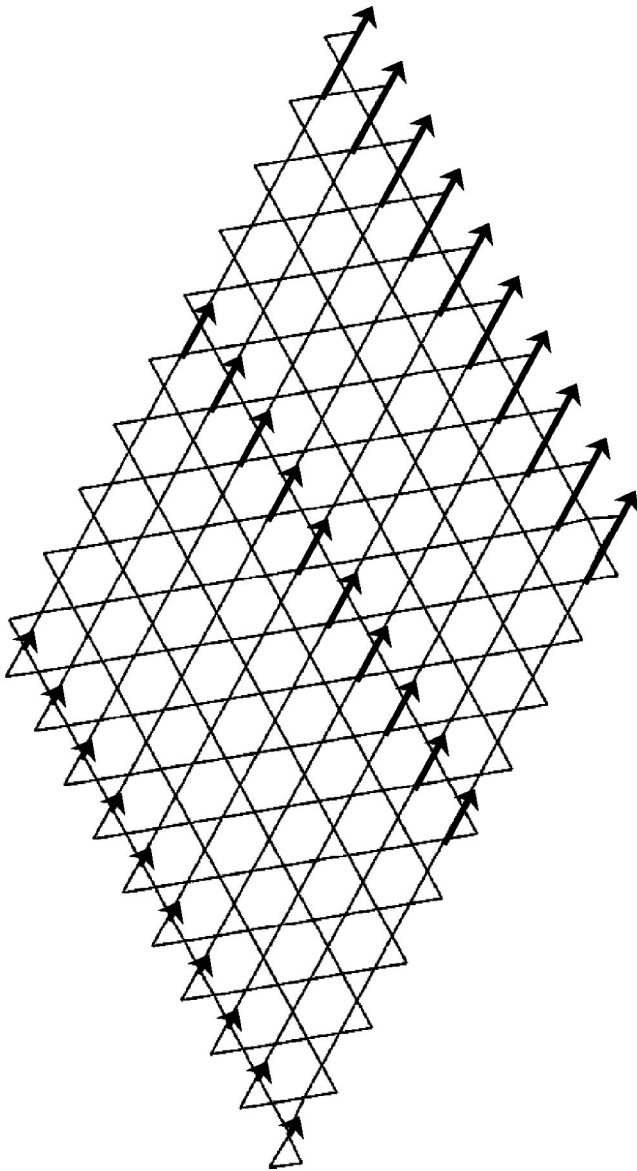


Fig. 6 The target displacement field described by  $u_d = A_0 \xi e_\zeta$

The strain energy of actuation is calculated in a straightforward manner depicted in Fig. 7. Consider an actuating member of length  $L$ , cross-sectional area  $A$ , and Young's modulus  $E$ . The imposed actuation strain of  $\varepsilon^T$  is the strain the member would undergo if the member were free to actuate (if the structure offered no resistance). As the structure will have some resistance to the actuation, the member will undergo some elastic strain that we denote  $\varepsilon^e$ . The axial force  $F$  experienced by the member is then easily calculated as  $F = \varepsilon^e EA$ . The work done by the actuator (acting on the structure) is the work of this axial force acting through the actuation strain  $\varepsilon^T$ ,  $-1/2 \varepsilon^e \varepsilon^T EAL$ , and it is stored as elastic strain energy in the structure.

**3.2 Reference Energy.** Now consider the work done by the same actuator, undergoing the same actuation strain  $\varepsilon^T$ , but in this case consider the structure to be rigid—that is, consider a structure that will completely resist the actuation. This corresponds to fixing both ends of the member as it is actuated. In this situation, the total strain of the member is zero, so  $\varepsilon^e + \varepsilon^T = 0$ . The energy

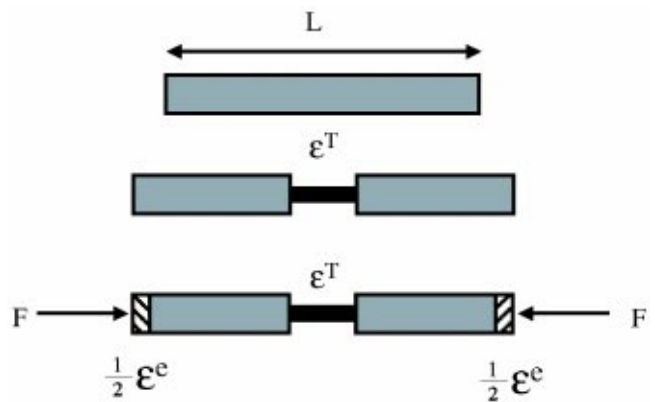


Fig. 7 The energy of actuation of a beam. The rest of the structure resists the imposed actuation strain  $\varepsilon^T$ , generating an elastic strain of  $\varepsilon^e$  and an internal force  $F = \varepsilon^e EA$ .

of actuation in this case is therefore  $1/2(\varepsilon^T)^2 EAL$ , and this is chosen as the reference energy for each member in the energy calculations and comparisons below.

Actuation of multiple members does not pose any energy accounting difficulties—the total energy of actuation can be calculated by adding up the contributions from each individual member, with the elastic strain of each member calculated in response to all the actuations. In some circumstances, the work done by an individual member may be negative—the actuations of other members may result in the structure actually assisting, not resisting, an actuation. However, the overall energy of actuation will of course always be positive. Thus, the relevant energy ratio calculated for energy comparisons is

$$\hat{W} = \frac{\sum_{i=1}^{\#members} -\frac{1}{2} \varepsilon_i^e \varepsilon_i^T E_i A_i L_i}{\sum_{i=1}^{\#members} \frac{1}{2} (\varepsilon_i^T)^2 E_i A_i L_i} \quad (13)$$

This energy ratio  $\hat{W}$  is plotted for several slenderness ratios in Fig. 8 for the target displacement fields shown above. For a structure with energy storage dominated by bending energy,  $\hat{W}$  can be

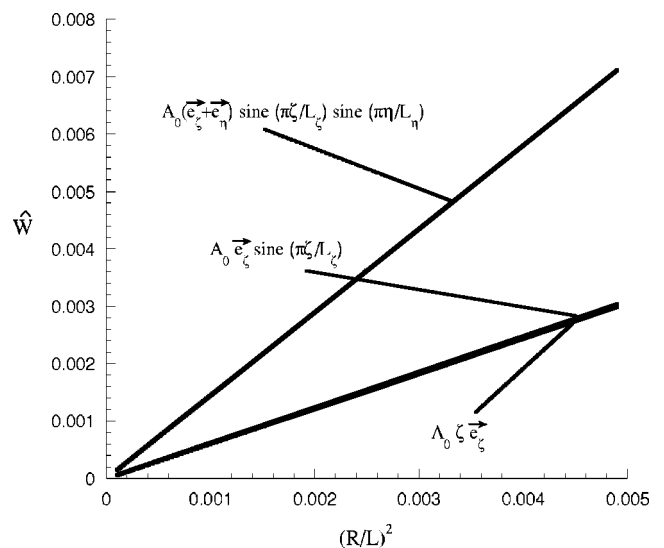
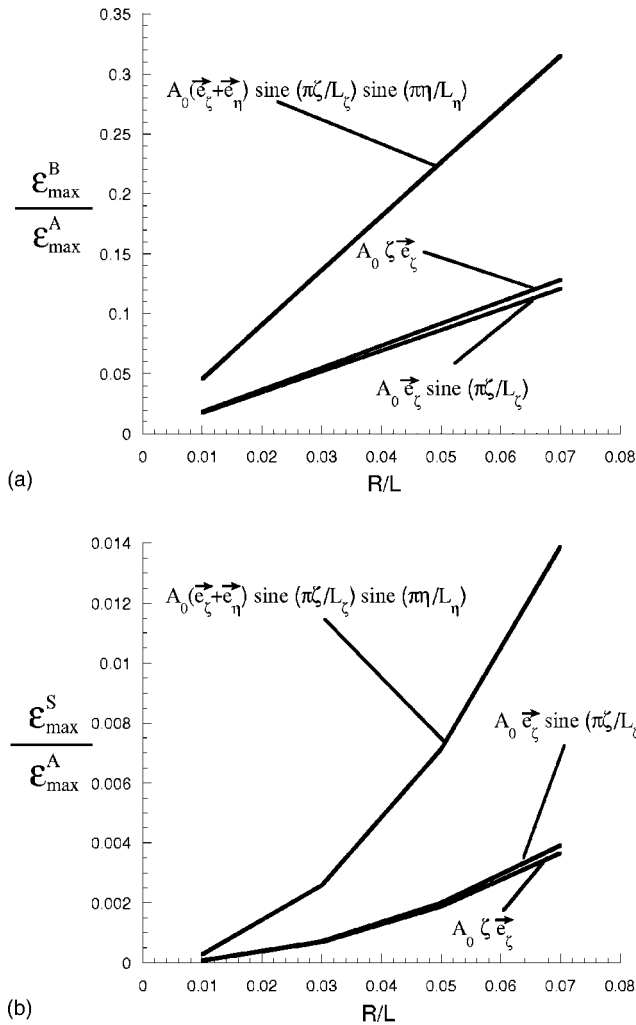


Fig. 8 Normalized actuation energy for the target displacement fields, as a function of  $(R/L)^2$



**Fig. 9 (a) Maximum bending strain normalized by maximum actuation strain for the target displacement fields, as a function of  $R/L$ . (b) Maximum stretching strain normalized by maximum actuation strain for the target displacement fields, as a function of  $R/L$ .**

shown to scale with the slenderness ratio squared,  $(R/L)^2$ , while for a statically overdetermined structure, such as a fully triangulated sheet,  $\hat{W}$  is expected to be of order unity, independent of the slenderness ratio and whether pin jointed or weld jointed. The energy associated with actuation of the Kagome structure is clearly much smaller than that energy of a fully triangulated truss grid. The energy associated with actuation of an isolated beam in a Kagome structure is investigated in work by Wicks and Guest [5]. For such actuations,  $\hat{W}$  scales linearly with slenderness, with energy equally partitioned between stretching and bending. However, for the target fields considered here,  $\hat{W}$  clearly scales as the square of the slenderness.

**3.3 Strain Levels Induced by Actuation.** As the structures will generally undergo cyclic actuations, investigation of strain levels for fatigue design is also required. One quantity of interest is the maximum stretching strain occurring in the structure divided by the maximum actuation strain. For a bending controlled structure, this ratio is also expected to scale with slenderness ratio squared. Of more interest is the ratio of maximum bending strain to maximum actuation strain—which is expected to scale linearly with the slenderness ratio for bending controlled structures. These trends are seen to hold in Fig. 9 where the normalized maximum

bending and stretching strains are plotted as a function of slenderness ratio for the target displacement fields described above. The maximum actuation strain,  $\epsilon_{\max}^A$ , is used to normalize the induced bending and stretching strains. The relatively larger bending strains will restrict the levels of actuation due to fatigue.

## 4 Kagome Plate Structure

**4.1 The Kagome Plate Structure.** Consider a solid face sheet of thickness  $t$ , backed by a planar Kagome structure. Core members attach to the face sheet and Kagome plane to form tetrahedral units, as shown in Fig. 2. The Kagome planar members and the core members have solid circular cross sections of radius  $R$  and are all of the same length  $L$ . As a result, the core thickness is  $H_c = \sqrt{2/3}L$ . While in some applications it may be desirable to use solid face sheets and Kagome planar sheets of different materials, for the purposes of this study we restrict the structure to be of one single isotropic material of Young's Modulus  $E$  and with a Poisson's ratio of  $\nu=1/3$ . The unit cell used in this analysis is shown in Fig. 2(c).

The stiffness matrix of the unit cell (Fig. 2(c)) of the Kagome plate structure is simulated through the use of a composite element comprised of beam and shell elements. We model the Kagome planar and core members as three-dimensional Euler-Bernoulli beams, with six degrees-of-freedom at each node. The behavior of the solid plate is simulated via linear shell elements in the commercial finite element package ABAQUS [8]. The in-plane behavior of these elements is plane stress, while the out-of-plane behavior corresponds with linear plate theory, [9], as these are flat shell elements.

Since the sandwich plate will generally be subject to applied transverse loads, the Kagome planar truss in its role as a face sheet must carry substantial in-plane loads in addition to undergoing actuation. For the sandwich plate to carry transverse loads efficiently, it is desirable for the solid and Kagome plane face sheets to have comparable in-plane stiffness. The in-plane stiffness of the Kagome planar truss is isotropic, with the relation between average in-plane strains and the overall stress resultants given by

$$\begin{aligned} \epsilon_{11} &= S^{-1}(N_{11} - \nu N_{22}), & \epsilon_{22} &= S^{-1}(N_{22} - \nu N_{11}), \\ \epsilon_{12} &= S^{-1}(1 + \nu)N_{12} \end{aligned} \quad (14)$$

with  $S = EA/(\sqrt{3}L)$  and  $\nu=1/3$ . Equating the in-plane stiffness of the solid sheet and that of the Kagome sheet described by (14) leads to the following relation between the face sheet thickness and member radius:

$$\frac{t}{L} = \frac{\pi}{\sqrt{3}} \left( \frac{R}{L} \right)^2. \quad (15)$$

This relation will be used to specify the face sheet thickness for the various member radii used in the examples detailed below.

**4.2 Actuation and Periodicity of the Infinite Kagome Plate.** First consider an infinite Kagome plate structure. The objective of this section is to probe how well the shape of the solid face sheet can be controlled by periodic actuations of the members of the planar Kagome face sheet. Actuation is simulated via the same cut-stress-reweld scheme outlined in Section 2.2. For the infinite plate, periodic target and actuation fields are considered and a corresponding periodic cell is adopted for performing the computations. The details of the periodic boundary conditions for out of plane behavior are given in the Appendix. The periodic boundary conditions, in addition to those suppressing rigid-body motions, are imposed via the use of Lagrangian multipliers, as shown in Section 2.3, resulting in solutions that show periodicity of the forces and moments exerted on the boundaries of the periodic cell.

As in the planar Kagome case, a simulation is run for a unit elongation of every member of the Kagome plane. Core members



Fig. 10 Periodic cell used for Kagome plate simulation

are not actuated. In this case, the vertical displacements of the nodes of the solid face sheet are assembled into a matrix of influence coefficients  $\mathbf{B}$ . The  $ij$ th component of  $\mathbf{B}$  is the vertical displacement of the  $i$ th node of the solid face sheet resulting from a unit elongation of the  $j$ th member of the Kagome plane.

The linearity of the theory allows the displacements of the nodes from arbitrary actuation (elongation or contraction) of any combination of members to be calculated easily once  $\mathbf{B}$  is assembled:

$$w_i = B_{ij} e_j \quad (16)$$

where  $\mathbf{e}$  is the vector of member actuations and  $\mathbf{w}$  the vector of vertical displacements of solid face sheet nodes.

Now consider a target field of the vertical displacements of the solid face sheet displacement field  $\mathbf{w}^d$ . We wish to determine how well this field can be recreated by actuating members of the Kagome plane. The Moore-Penrose generalized inverse is employed in a similar manner as before to calculate elongations  $\tilde{\mathbf{e}}$  and displacements  $\tilde{\mathbf{w}}$  via the relations

$$\tilde{e}_i = B_{ij}^\dagger w_j^d \quad (17)$$

$$\tilde{w}_i = B_{ij} \tilde{e}_j \quad (18)$$

where  $\mathbf{B}^\dagger$  is the Moore-Penrose generalized inverse of  $\mathbf{B}$ . Here,  $\tilde{\mathbf{e}}$  is the vector of member actuations which minimize the squared error between  $\tilde{\mathbf{w}}$  and  $\mathbf{w}^d$ . As before, if there exist multiple vectors of actuations which minimize this squared error,  $\tilde{\mathbf{e}}$  is such a vector of minimal length.

**4.3 Example Target Displacement Fields.** The simulations outlined above were run for several target displacement fields. The periodic cell used for these simulations is shown in Fig. 10. It contains a total of 64 unit cells. The axes used for describing the displacements fields described here are the same  $\zeta$ -axis and  $\eta$ -axis used in the planar Kagome examples. It is important to note that the target displacement fields imposed are all consistent with the periodic displacement boundary conditions described in the Appendix. As in the planar Kagome examples, the displacements themselves are not, in general, periodic, while the stresses, strains and curvatures are periodic. Here we consider, for example, a displacement field corresponding to a constant curvature—the internal forces are periodic (with periodicity size of the periodic cell), while the displacements are clearly not periodic.

The first target displacement field is described by

$$\mathbf{w}^d = A_0 \zeta^2 \mathbf{e}_z \quad (19)$$

Here, the displacement corresponds to the vertical displacement of the nodes of the solid face sheet corresponding to a state of constant curvature of  $\kappa_{\zeta\zeta} = 2A_0$  with  $A_0$  as the amplitude factor and  $\mathbf{e}_z$  the unit vector perpendicular to the plate (aligned with the  $z$ -axis). The Moore-Penrose best-fit actuations for this displacement field are calculated as described above. The achievable displacement field is shown in Fig. 11—only the achievable field is shown, as it is indistinguishable from the target field. There are 384 members that are actuated in this simulation and only 209 target nodal displacements. However, the rank of  $\mathbf{B}$  is only 194, so it is interesting that the achievable field is so close to the target field. Actuation energy and strains will be discussed in Section 5.

The second target displacement field is

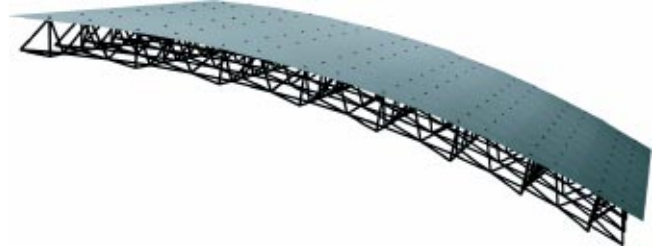


Fig. 11 Best-fit displacement field calculated using Moore-Penrose analysis for target field  $\mathbf{w}^d = A_0 \zeta^2 \mathbf{e}_z$

$$\mathbf{w}^d = A_0 \mathbf{e}_z \sin\left(\frac{2\pi\zeta}{L_\zeta}\right) \quad (20)$$

where  $L_\zeta$  is the length of the unit cell in the  $\zeta$ -direction. This displacement field has zero displacement along two edges of the periodic cell, corresponding to  $\zeta=0$  and  $\zeta=L_\zeta$ . Along these same edges, the slope in the  $\zeta$ -direction takes the value of  $2\pi A_0/L_\zeta$ . This displacement field takes on a maximum value of  $\pm A_0 \mathbf{e}_z$  at  $\zeta=L_\zeta/4$  and  $\zeta=3L_\zeta/4$ . The achievable displacement field shown in Fig. 12 again matches the target field.

One final target displacement field of interest is described by

$$\mathbf{w}^d = A_0 \mathbf{e}_z \sin\left(\frac{2\pi\zeta}{L_\zeta}\right) \sin\left(\frac{2\pi\eta}{L_\eta}\right) \quad (21)$$

Note that, unlike the previous target displacement fields, this field involves a nonzero Gaussian curvature of the solid face sheet. The achievable field shown in Fig. 13 also matches the target field.

#### 4.4 Comparison With Long Wavelength Theory.

The best-fit actuations for the displacement fields described above have been compared with the actuations predicted by the long wavelength approximation outlined in previous work, [1]. In this long wavelength theory, the extensional strain,  $\boldsymbol{\varepsilon}^T$ , of a member is  $\boldsymbol{\varepsilon}^T = -H \boldsymbol{\kappa}_{\alpha\beta}^d t_\alpha t_\beta$  where  $\boldsymbol{\kappa}^d$  is the curvature tensor associated with  $\mathbf{w}^d$  ( $\kappa_{\alpha\beta}^d = w_{,\alpha\beta}^d$ ) and  $t_\alpha$  is the unit vector specifying the orientation of the member.

Member actuations calculated via the Moore-Penrose analysis for the case of constant curvature agree well with actuations predicted by the long wavelength theory. As this is a displacement field with infinite wavelength, the agreement is not surprising. Actuations for the simulation corresponding to the sinusoidal dis-



Fig. 12 Best-fit displacement field calculated using Moore-Penrose analysis for target field  $\mathbf{w}^d = A_0 \mathbf{e}_z \sin(2\pi\zeta/L_\zeta)$

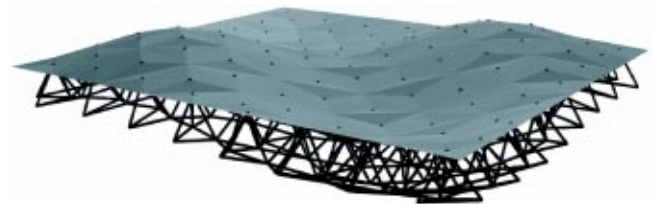


Fig. 13 Best-fit displacement field calculated using Moore-Penrose analysis for target field  $\mathbf{w}^d = A_0 \mathbf{e}_z \sin(2\pi\zeta/L_\zeta) \times \sin(2\pi\eta/L_\eta)$ . The faceting of the solid sheet is an artifact of the plotting—the actual shape of the solid sheet is smooth.

placement field (20) are also predicted well by the long wavelength theory. This displacement field has a wavelength of eight unit cells. Actuators were also calculated for a sinusoidal displacement field with a wavelength of only four unit cells:

$$\mathbf{w}^d = A_0 \mathbf{e}_z \sin\left(\frac{4\pi\zeta}{L_\zeta}\right). \quad (22)$$

The actuators predicted by the long wavelength theory show more discrepancy in this case, as would be expected, but the largest actuation strains are not in major disagreement.

**4.5 Actuation of Selected Kagome Members.** As a practical matter, it will usually be the case that only a small subset of the Kagome face members will be actuated. The Moore-Penrose actuation scheme described previously can still be used to probe how well such structures can achieve the target displacement fields.

Consider there are only  $M$  members which have been identified for actuation. The matrix  $\mathbf{B}$  contains the displacements of the solid face sheet nodes corresponding to all member actuations. Thus, we can construct a new matrix  $\mathbf{B}^*$  that contains only the  $M$  columns corresponding to the members to be actuated. Then the vertical displacements of the face sheet nodes are again easily calculated according to

$$w_i = B_{ij}^* e_j^* \quad (23)$$

where now  $\mathbf{e}^*$  is the vector of actuations of those members that can be actuated.

Consider a target displacement field  $\mathbf{w}^d$ . The minimum length, minimum squared error set of actuations for the  $M$  members is

$$\tilde{e}_i^* = B_{ij}^{*\dagger} w_j^d. \quad (24)$$

Here,  $\mathbf{B}^{*\dagger}$  is the Moore-Penrose generalized inverse of  $\mathbf{B}^*$ . The vertical displacements of the solid face nodes are also easily calculated:

$$\tilde{w}_i = B_{ij}^* \tilde{e}_j^*. \quad (25)$$

Reconsider the target displacement field that corresponds to constant curvature:

$$\mathbf{w}^d = A_0 \zeta^2 \mathbf{e}_z. \quad (26)$$

Now, however, assume that only members of the Kagome plane in the row corresponding to  $\zeta \approx L_\zeta/2$  can actuate. These members are located in the middle of the periodic cell, as shown in Fig. 14(a). The Moore-Penrose best-fit displacement field is shown in Fig. 15. Note that the structure displays only local curvature along the line  $\zeta = L_\zeta/2$ .

Reconsider also the target sinusoidal displacement field:

$$\mathbf{w}^d = A_0 \mathbf{e}_z \sin\left(\frac{2\pi\zeta}{L_\zeta}\right). \quad (27)$$

Here, however, assume that only the selected members of the Kagome plane are actuated corresponding to those aligned in rows having  $\zeta \approx L_\zeta/4$  and  $\zeta \approx 3L_\zeta/4$ , as shown in Fig. 14(b). These members lie within the zones of maximum curvature magnitude of the target displacement field. When the Moore-Penrose analysis is run under these conditions, the resulting displacement field is displayed in Fig. 16. While the shape looks very similar to that in Fig. 12 achieved by activating all the members of the Kagome face, the curvature in Fig. 16 is nevertheless limited to regions where members are actuating along  $\zeta \approx L_\zeta/4$  and  $\zeta \approx 3L_\zeta/4$ .

## 5 Energy of Actuation of Kagome Plate Structure

**5.1 Energy of Actuation.** The strain energy of actuation is again calculated in the manner depicted in Fig. 7 and the work done by each actuator is  $-1/2 \varepsilon^e \varepsilon^T EAL$  where  $\varepsilon^T$  is its actuation strain and  $\varepsilon^e$  is the elastic strain it experiences as a consequence of all actuations. This work is stored as elastic strain energy in the

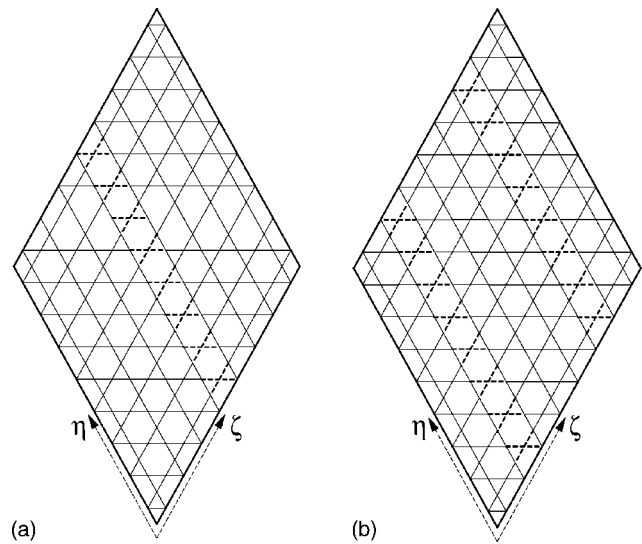


**Fig. 14** The members which are allowed to actuate in the analysis of actuation of selected Kagome members. Only the Kagome plane is shown. The dashed members are the members selected to actuate.

structure. The work done by the same actuator, undergoing the same actuation strain  $\varepsilon^T$ , in a perfectly stiff structure is, as before,  $1/2(\varepsilon^T)^2 EAL$ . This energy is taken as the reference energy for the energy calculations presented below. As with the planar Kagome truss, actuation of multiple members does not pose any energy accounting difficulties—the total energy of actuation can be calculated by adding up the contributions from each individual member. The relevant energy ratio calculated for energy comparisons is again given by (13) where  $\varepsilon_i^e$  are computed for each specific set of actuations  $\varepsilon_i^T$ .

As noted earlier, for a structure with energy storage dominated by bending energy in the beam members, the energy ratio  $\hat{W}$  can be shown to scale with the slenderness ratio squared,  $(R/L)^2$ . It is important to note that the sandwich plate comprised of the Kagome face with a solid face sheet is indeterminate—not only are the joints welded, but a solid face is intrinsically indeterminate. It can be anticipated that this indeterminacy will result in

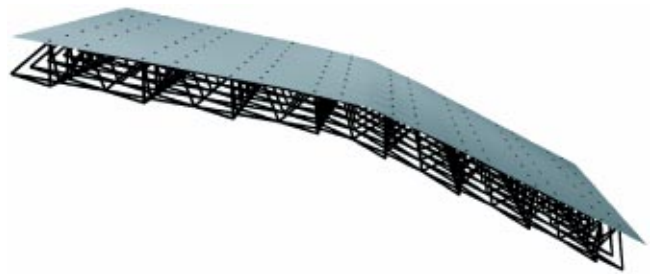


**Fig. 15** The best-fit displacement field when limited members are allowed to actuate for the target displacement field  $\mathbf{w}^d = A_0 \zeta^2 \mathbf{e}_z$



**Fig. 16** The best-fit displacement field when limited members are allowed to actuate for the target displacement field  $\mathbf{w}^d = A_0 \mathbf{e}_z \sin(2\pi\zeta/L_\zeta)$

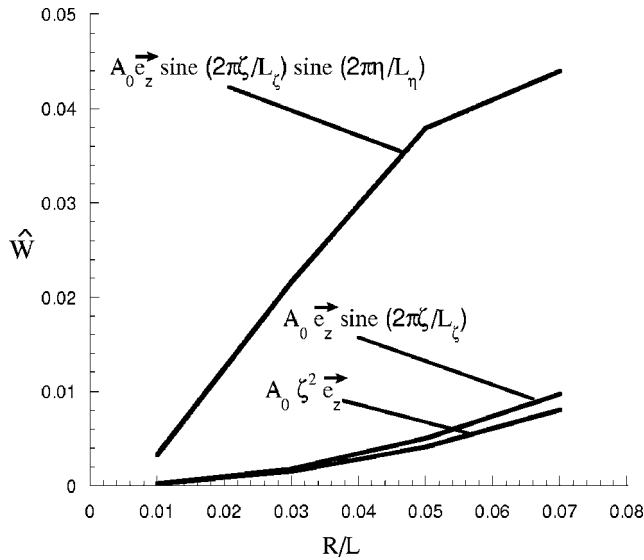


Fig. 17 Normalized actuation energy for the target displacement fields, as a function of  $R/L$

somewhat larger actuation energies than those predicted for bending dominated structures. The energy ratio  $\hat{W}$  is plotted against the slenderness ratio for the truss members in Fig. 17 for the three target periodic displacement fields described above. It is clear from this plot that the Kagome-backed sandwich plate offers considerably more resistance to actuation for modes with curvature in two directions than to actuations that bend the plate solely in one direction. Nevertheless, compared to the reference energy, the actuation energy is still small. A more meaningful interpretation of the actuation energy will be given in Section 5.2. Similar trends are seen in Figs. 18 and 19, where the maximum bending and stretching strain quantities for these displacement fields are plotted as a function of slenderness ratio.

Plates actuated to produce double curvature will necessarily be limited to smaller actuation strains (and thus displacements) to ensure they do not undergo plastic yield. It is important to note that the results here for the double curvature plate have been computed using linear theory. Large resistance will arise for suffi-

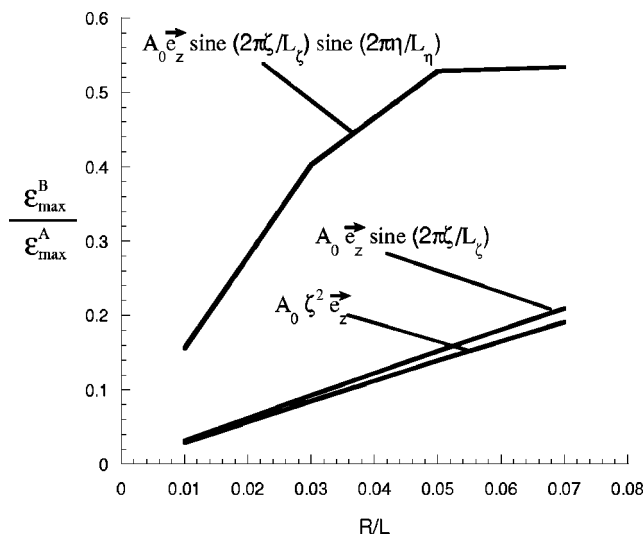


Fig. 18 Maximum bending strain normalized by maximum actuation strain for the target displacement fields, as a function of  $R/L$

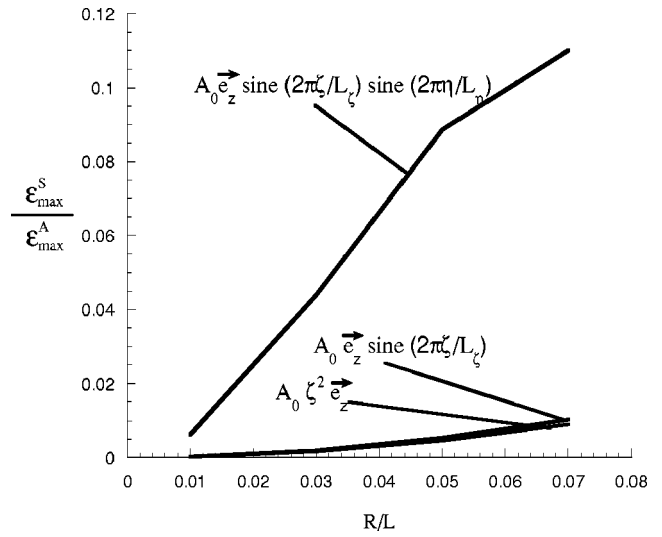


Fig. 19 Maximum stretching strain normalized by maximum actuation strain for the target displacement fields, as a function of  $R/L$

ciently large deflections due to nonlinear coupling between bending and stretching in the solid face sheet whenever shapes with nonzero Gaussian curvature are actuated. This nonlinear effect is not considered in this paper. Thus, the results for doubly curved shapes presented here are restricted to small deflections.

**5.2 Comparison of Two Energy Quantities.** In most applications, a multifunctional role of these actuating structures is anticipated where the structures will be required to both change shape and carry and lift significant loads. Here an approximate calculation is presented of the relative energies to perform these two different functions, highlighting the significance of structures with low resistance to actuation.

For specificity, consider a cantilevered Kagome plate structure of length  $\ell$  subjected to a load per unit length  $P$  at free end. Now imagine that, via actuation of Kagome members, the cantilevered end is raised a distance  $\delta_A$ . The work per unit length done to raise this load scales as

$$W_P \approx P \delta_A = P \epsilon_A \ell \quad (28)$$

where  $\epsilon_A$  is the typical actuation strain for a member near the clamped end. The energy per unit length stored as strain energy in the Kagome plate structure due to resistance to actuation scales as

$$W_A \approx kEA \epsilon_A^2 \quad (29)$$

where  $A$  is the member cross-sectional area and  $k$  is a small fraction of unity for structures with low internal resistance to actuation, such as those reported above.

The structure must be designed to be able to carry the load per unit length  $P$ . For an optimally designed structure, we anticipate that face yielding or buckling will be an active constraint, [10]. With  $\sigma_c$  as the critical stress in a Kagome member (set by either buckling or yielding), the member must be sized to satisfy a relation that scales as  $\sigma_c AL \approx PL \ell$ . Thus, to carry the applied load, the member cross-sectional area will be sized according to the scaling law

$$A \approx P \ell / \sigma_c. \quad (30)$$

The maximum allowable actuation is also related to this critical stress  $\sigma_c$  according to

$$\epsilon_A \approx f \sigma_c / E. \quad (31)$$

Here,  $f$  is the factor relating actuation strain and the maximum strain induced in the structure due to actuation as plotted for the

Kagome structures earlier in the paper. In most instances, the condition limiting actuation is likely to be yielding in bending, at least for the Kagome structures, but the possibility of buckling of members under compression must also be considered. Now calculate the ratio of the energy stored in the structure due to actuation to the amount of energy required to raise the load:

$$\frac{W_A}{W_P} \approx \frac{kEP\ell \varepsilon_A^2 / \sigma_c}{P\varepsilon_A \ell} = \frac{k(E/\sigma_c) \varepsilon_A^2}{\varepsilon_A} = kf. \quad (32)$$

For the Kagome sandwich plates analyzed in Section 4, typical values of  $f$  are about 10, as the maximum induced bending strains in the Kagome plane are about 10% of the maximum actuation strain. Values of  $k$  depend upon the specifics of the actuation, but because of their low resistance to actuation they typically range from about 1/100 to 1/1000 for the Kagome structures. Thus, for such structures, the energy required to raise the applied loads will be 10–100 times the energy stored as strain energy in the structure. The sandwich plates subject to double curvature offer somewhat more internal resistance to actuation ( $k \approx 1/40$ ), but values of  $f$  are also lower ( $f \approx 2$ ) such that the energy stored in internal resistance is still relatively low, i.e.,  $W_A/W_P \approx 1/20$ . In this fundamental sense, the Kagome plate structure offers minimal internal resistance to the actuation.

## 6 Concluding Remarks

Sandwich plates employing as the actuation plane a Kagome planar truss have been studied to assess their effectiveness and efficiency in the dual role of a load carrying structure capable of actuated shape changes. The advantage of the Kagome planar truss in this application is its in-plane stiffness and strength coupled with its low internal resistance to actuation. The sandwich plate offers more internal resistance than the isolated Kagome plane. Nevertheless, an actuated plate designed to carry specific loads can achieve a wide variety of shapes with relatively low expenditure of energy to overcome the internal resistance compared to the work expended in raising the loads. It remains to be seen from prototypes that are currently under construction, as well as from further theoretical work, just how large the actuated amplitudes can be and the range of modes shapes that can be produced. This is especially true for double curvature modes that require greater expenditure of energy to overcome internal resistance.

## Acknowledgments

This work was supported by the grant Multifunctional Mechano-Electronic Materials (N00014-01-1-0523) and by the Division of Engineering and Applied Sciences, Harvard University.

## Appendix

**Periodic Displacement Boundary Conditions.** Consider a periodic structure such as that shown in Fig. A1. With A as the reference periodic cell and  $\mathbf{r}^{(i)}$  the vector from the origin in A to the  $i$ th node in A, we denote the displacements of the nodes in A as

$$\mathbf{u}_A^{(i)} = \mathbf{u}_0^{(i)}. \quad (A1)$$

Let B, C, and D be neighboring periodic cells, as shown in Fig. A1. We denote the displacements at the nodes in those cells as

$$\mathbf{u}_B^{(i)} = \mathbf{u}_0^{(i)} + \mathbf{u}_{BA} + \boldsymbol{\omega}_{BA} \times \mathbf{r}^{(i)} \quad (A2)$$

$$\mathbf{u}_C^{(i)} = \mathbf{u}_0^{(i)} + \mathbf{u}_{CA} + \boldsymbol{\omega}_{CA} \times \mathbf{r}^{(i)} \quad (A3)$$

$$\mathbf{u}_D^{(i)} = \mathbf{u}_0^{(i)} + \mathbf{u}_{DA} + \boldsymbol{\omega}_{DA} \times \mathbf{r}^{(i)} \quad (A4)$$

$$\mathbf{u}_D^{(j)} = \mathbf{u}_0^{(j)} + \mathbf{u}_{CA} + \boldsymbol{\omega}_{CA} \times \mathbf{r}^{(j)}. \quad (A5)$$

Combining (A4) with (A3) or (A5) with (A2) yields

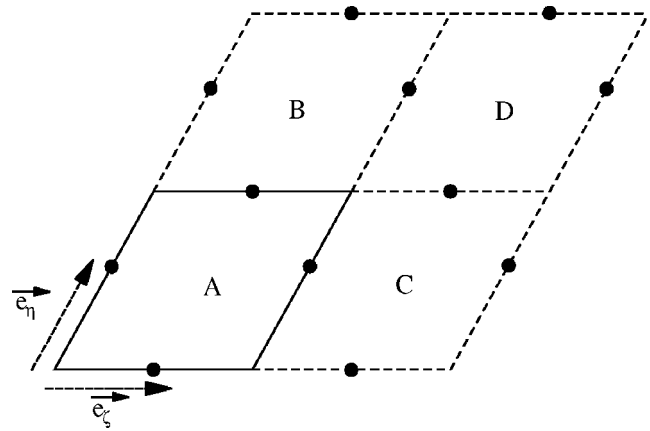


**Fig. A1 A periodic structure. A, B, C, D are equivalent periodic cells. The dots correspond to nodes along the edges of the periodic cells.  $\mathbf{e}_\zeta$  and  $\mathbf{e}_\eta$  are unit vectors sligned with the edges of the periodic cells.**

$$\mathbf{u}_D^{(i)} = \mathbf{u}_0^{(i)} + \mathbf{u}_{BA} + \mathbf{u}_{CA} + (\boldsymbol{\omega}_{BA} + \boldsymbol{\omega}_{CA}) \times \mathbf{r}^{(i)}. \quad (A6)$$

Now consider the rotations at each node in A. Denote these as

$$\boldsymbol{\phi}_A^{(i)} = \boldsymbol{\phi}_0^{(i)}. \quad (A7)$$

Similarly for B, C, and D:

$$\boldsymbol{\phi}_B^{(i)} = \boldsymbol{\phi}_0^{(i)} + \boldsymbol{\omega}_{BA} \quad (A8)$$

$$\boldsymbol{\phi}_C^{(i)} = \boldsymbol{\phi}_0^{(i)} + \boldsymbol{\omega}_{CA} \quad (A9)$$

$$\boldsymbol{\phi}_D^{(i)} = \boldsymbol{\phi}_0^{(i)} + \boldsymbol{\omega}_{BA} + \boldsymbol{\omega}_{CA}. \quad (A10)$$

Now consider the edge joining cell A and cell B. With the displacements of the nodes along the top of A equal to the displacements of the nodes along the bottom of B:

$$\mathbf{u}_0^{(j)} = \mathbf{u}_0^{(i)} + \mathbf{u}_{BA} + \boldsymbol{\omega}_{BA} \times \mathbf{r}^{(i)}. \quad (A11)$$

Here, (J) is along the top of A and (i) along the bottom of B.

We can write  $\mathbf{r}^{(j)} = \mathbf{r}^{(i)} + L_\eta \mathbf{e}_\eta$ , where  $L_\eta$  is the length of the periodic cell in the  $\mathbf{e}_\eta$  direction.

Now, equate the displacements along the edge joining C and D:

$$\mathbf{u}_0^{(j)} + \mathbf{u}_{CA} + \boldsymbol{\omega}_{CA} \times \mathbf{r}^{(j)} = \mathbf{u}_0^{(i)} + \mathbf{u}_{CA} + \mathbf{u}_{BA} + (\boldsymbol{\omega}_{BA} + \boldsymbol{\omega}_{CA}) \times \mathbf{r}^{(i)}. \quad (A12)$$

Rearranging and simplifying (A12) leads to:

$$\mathbf{u}_0^{(j)} - \mathbf{u}_0^{(i)} = \mathbf{u}_{BA} + \boldsymbol{\omega}_{BA} \times \mathbf{r}^{(i)} - \boldsymbol{\omega}_{CA} \times L_\eta \mathbf{e}_\eta \quad (A13)$$

Comparison of (A13) with (A11) above yields:

$$\boldsymbol{\omega}_{CA} \times L_\eta \mathbf{e}_\eta = 0 \Rightarrow \boldsymbol{\omega}_{CA} = \omega_{CA} \mathbf{e}_\eta \quad (A14)$$

Now equate the displacements of nodes along the edge between cells A and C:

$$\mathbf{u}_0^{(j)} = \mathbf{u}_0^{(j)} + \mathbf{u}_{CA} + \boldsymbol{\omega}_{CA} \times \mathbf{r}^{(j)} \quad (A15)$$

Here, (J) is along the right of A and (j) along the left of C.

Now we can write  $\mathbf{r}^{(j)} = \mathbf{r}^{(j)} + L_\zeta \mathbf{e}_\zeta$ , where  $L_\zeta$  is the length of the periodic cell in the  $\mathbf{e}_\zeta$  direction.

Equating displacements of nodes along the edge between cells B and D yields

$$\begin{aligned} \mathbf{u}_0^{(j)} + \mathbf{u}_{BA} + \boldsymbol{\omega}_{BA} \times (\mathbf{r}^{(j)} + L_\zeta \mathbf{e}_\zeta) \\ = \mathbf{u}_0^{(j)} + \mathbf{u}_{CA} + \mathbf{u}_{BA} + (\boldsymbol{\omega}_{BA} + \boldsymbol{\omega}_{CA}) \times \mathbf{r}^{(j)}. \end{aligned} \quad (A16)$$

Rearranging and simplifying (A16) yields:

$$\mathbf{u}_0^{(j)} - \mathbf{u}_0^{(j)} = \mathbf{u}_{CA} + \boldsymbol{\omega}_{CA} \times \mathbf{r}^{(j)} - \boldsymbol{\omega}_{BA} \times L_\zeta \mathbf{e}_\zeta. \quad (A17)$$

Comparison of (A17) with (A15) with above yields

$$\boldsymbol{\omega}_{BA} \times L_{\zeta} \mathbf{e}_{\zeta} = 0 \Rightarrow \boldsymbol{\omega}_{BA} = \boldsymbol{\omega}_{BA} \mathbf{e}_{\zeta}. \quad (A18)$$

So, for edges parallel to  $\mathbf{e}_{\zeta}$ , displacements are related by

$$\mathbf{u}_0^{(j)} - \mathbf{u}_0^{(i)} = \mathbf{u}_{BA} + \boldsymbol{\omega}_{BA} \mathbf{e}_{\zeta} \times \mathbf{r}^{(i)}. \quad (A19)$$

Now, write  $\mathbf{r}^{(i)} = \zeta^{(i)} \mathbf{e}_{\zeta} + z^{(i)} \mathbf{k}$  and note that  $\mathbf{k}$  is perpendicular to  $\mathbf{e}_{\zeta}$  and  $\mathbf{e}_{\eta}$ .

Thus, we can write

$$\mathbf{u}_0^{(j)} - \mathbf{u}_0^{(i)} = \mathbf{u}_{BA} + \boldsymbol{\omega}_{BA} z^{(i)} \mathbf{e}_{\zeta} \times \mathbf{k}. \quad (A20)$$

Thus, for all pairs of points the same distance above the reference plane

$$\mathbf{u}_0^{(j)} - \mathbf{u}_0^{(i)} = \mathbf{u}_{BA} = \mathbf{u}_0^{(j+m)} - \mathbf{u}_0^{(i+m)}. \quad (A21)$$

Similar along the edges parallel to  $\mathbf{e}_{\eta}$ :

$$\mathbf{u}_0^{(j)} - \mathbf{u}_0^{(i)} = \mathbf{u}_{CA} = \mathbf{u}_0^{(j+m)} - \mathbf{u}_0^{(i+m)}. \quad (A22)$$

Now, compare the rotations. Setting equal the rotations at nodes along the edge joining cells A and B:

$$\boldsymbol{\phi}_0^{(j)} = \boldsymbol{\phi}_0^{(i)} + \boldsymbol{\omega}_{BA} = \boldsymbol{\phi}_0^{(i)} + \boldsymbol{\omega}_{BA} \mathbf{e}_{\zeta}. \quad (A23)$$

Equating rotations at nodes along the edge joining cells C and D:

$$\boldsymbol{\phi}_0^{(j)} + \boldsymbol{\omega}_{CA} = \boldsymbol{\phi}_0^{(i)} + \boldsymbol{\omega}_{BA} + \boldsymbol{\omega}_{CA} \quad (\text{same as (A23)}). \quad (A24)$$

Finally, equating rotations at nodes along the edge joining cells A and C:

$$\boldsymbol{\phi}_0^{(j)} = \boldsymbol{\phi}_0^{(i)} + \boldsymbol{\omega}_{CA} = \boldsymbol{\phi}_0^{(i)} + \boldsymbol{\omega}_{CA} \mathbf{e}_{\eta}. \quad (A25)$$

## References

- [1] Hutchinson, R. G., Wicks, N., Evans, A. G., Fleck, N. A., and Hutchinson, J. W., 2003, "Kagome Plate Structures for Actuation," *Int. J. Solids Struct.*, **40**, pp. 6969–6980.
- [2] Hutchinson, R. G., and Fleck, N. A., 2003, in preparation.
- [3] Hyun, S., and Torquato, S., 2002, "Optimal and Manufacturable Two-Dimensional Kagome-Like Cellular Solids," *J. Mater. Res.*, **17**, pp. 137–144.
- [4] Guest, S. D., and Hutchinson, J. W., 2003, "On the Determinacy of Repetitive Structures," *J. Mech. Phys. Solids*, **51**, pp. 383–391.
- [5] Wicks, N., and Guest, S. D., 2003, "Single Member Actuation in Large Repetitive Truss Structures," *Int. J. Solids Struct.*, **41**, pp. 965–978.
- [6] Eshelby, J. D., 1957, "The Determination of the Elastic Field of an Ellipsoidal Inclusion, and Related Problems," *Proc. R. Soc. London, Ser. A*, **241**, pp. 376–396.
- [7] Strang, G., 1988, *Linear Algebra and its Applications*, Harcourt Brace Jovanovich, Orlando, FL.
- [8] Hibbit, Karlsson, and Sorensen, Inc., 2002, ABAQUS Version 6.3.
- [9] Timoshenko, S. P., and Gere, J. M., 1961, *Theory of Elastic Stability*, McGraw-Hill, New York.
- [10] Wicks, N., and Hutchinson, J. W., 2001, "Optimal Truss Plates," *Int. J. Solids Struct.*, **38**, pp. 5165–5183.